*Technical Note*

# A Nonlinear Radiometric Normalization Model for Satellite Imgaes Time Series based on Artificial Neural Networks and Greedy Algroithm

**Zhaohui Yin [1], Jiayu Sun [1], Haoran Zhang [1], Wenyi Zhang [1], Lejun Zou [1,*] and Xiaohua Shen [1,*]**

[1] School of Earth Sciences, Zhejiang University, 38 Zheda Road, Hangzhou 310027, China; zhyin@zju.edu.cn (Z. Yin); sunjy2016@zju.edu.cn (J. Sun); zhanghr5@mail2.sysu.edu.cn (H.Zhang); 3170101586@zju.edu.cn (W. Zhang)

* Correspondence: shenxh@zju.edu.cn (X. Shen); zoulejun2006@zju.edu.cn (L. Zou)

**Abstract:** Satellite Image Time Series (SITS) is a data set which includes satellite images across several years with a high acquisition rate. Radiometric normalization is a fundamental and important preprocessing method for remote sensing applications using SITS due to the radiometric distortion caused by noise between images. Normalizing the subject image based on the reference image is a general strategy when using traditional radiometric normalization methods to normalize multi-temporal imagery (usually two scenes or three scenes in different time phases). However, these methods are not suitable for calibrating SITS because they cannot minimize the radiometric distortion between any pair of images in SITS. The existing relative radiometric normalization methods for SITS are based on linear assumptions which cannot effectively reduce nonlinear radiometric distortion caused by continuously changing noise in SITS. To overcome this problem and obtain a more accurate SITS, this study proposed a Nonlinear Radiometric Normalization Model (named NMAG) for SITS based on Artificial Neural Networks (ANN) and Greedy Algroithm (GA) . In this method, GA was used to determine the correction order of SITS and calculate the error between the image to be corrected and normalized images, which avoided the selection of a single reference image. ANN was used to obtain the optimal solution of error function, which minimized the radiometric distortion between different images in SITS. SITS composed of 21 Landsat-8 images in Tianjin City from October 2017 to January 2019 were selected to test the method. We compared NMAG with other two contrasting method (refered as CM1 and CM2), and found that the average of root mean square error $(\mu_{RMSE})$ of NMAG $(497.22)$ was significantly smaller than those of CM1 $(641.39)$ and CM2 $(543.47)$, and the accuracy of normalized SITS obtained by using NMAG has increased by 22.4% and 8.5% toward CM1 and CM2, respectively. These experimental results confirmed the effectiveness of NMAG in the reduction of radiometric distortion caused by continuously changing noise between images in SITS.

**Keywords:** Satellite Image Time Series; Radiometric Normalization; Nonlinear Radiometric Distortion; Artificial Neural Networks

## 1. Introduction

Satellite Image Time Series (SITS) can provide abundant information to describe temporal changes of the generation and development of ground features in an area. It was used as an important data source in many fields such as environmental monitoring, land cover change monitoring, crop growth monitoring and so on [1–3]. However, the temporal information extracted from SITS is inevitably disturbed by noise unrelated to ground features, such as atmospheric absorption and scattering, sensor-target illumination geometry, sensor calibration, etc., which will lead to inaccurate results of remote sensing applications [4]. Thus, radiometric normalization is required prior to any applications using SITS.

Radiometric calibration can be classified into absolute radiometric calibration and relative radiometric calibration (also named relative normalization). Because it is usually difficult to obtain atmospheric properties, a relative radiometric calibration based on the

inherent radiometric information of images is alternative when absolute surface radiances are not needed [5]. In early research methods, global image statistics were utilized to derectly establish the gray value mapping relationship between the subject image and the reference image, such as Histogram Matching (HM), Mean-Standard deviation (MS) and so on [6,7]. However, these methods reduce the radiometric difference resulted from the variation of ground features while reducing the radiometric distortion caused by noise. Therefore, these methods are only suitable for image mosaicking due to the ambiguous result of the physical meaning of normalized images [8]. In order to address this issue effectively, methods based on regression model are developed, which is established by using a set of invariant pixels [9] (named pseudo-invariant features or PIFs) from the subject and reference images.

Linear regression models are simple and effective so that they have been widely used to minimize the radiometric distortion, such as simple linear regression model (SR), principal component analysis (PCA), Theil-Sen regression model and so on [10,11]. However, relative normalization methods based on linear assumptions are inappropriate for dealing with complex nonlinear radiometric distortions between the subject image and the reference image. The development of artificial intelligence technology, such as artificial neural network, genetic algorithms etc., provides an effective tool to deal with this problem [12,13].

The relative radiometric methods mentioned above are not suitable for calibrating SITS, because they are based on the reference image to implement the radiometric normalization of the subject image, which cannot minimize the radiometric distortion between any pair of images in SITS. Wu et al. developed a new radiometric normalization procedure for SITS to solve this issues effectively, which obtained a more objective and accurate correction results than previous methods [14]. However, continuously changing noise in SITS usually results in nonlinear radiometric distortion between images in reality, and the method proposed by Wu et al. cannot effectively reduce such nonlinear radiometric distortion.

An optimum method for minimizing nonlinear radiometric distortion between images in SITS is needed to facilitate remote sensing application. Thus, in this paper we constructed a nonlinear radiometric normalization model for SITS,in which an artificial neural network (ANN) and greedy algorithm(GA) are combined for the nonlinear radiometric normalization of SITS. Here, GA is used for determining the correction order of SITS and calculate the error function of the image to be corrected, and ANN is used for obtaining the optimal solution of error function. Hereinafter, this nonlinear radiometric normalization procedure is called NMAG model.

## 2. Description of methodology

The existing radiometric normalization approaches are based on the reference image $X_r$ to correct the subject image $X_c$. The key of these methods is to find a mapping function $f()$ to minimize the radiometric distortion between subject image $f(X_c)$ and reference image $X_r$. The objective function $Q_r$ can be expressed as:

$$Q_r = min \sum_{s \in S} [f(X_c^s - X_r^s)]^2 \quad (1)$$

where $S$ represents pseudo-invariant features (PIFs), $s \in S$ represents the pseudo-invariant features (PIF) in PIFs, $f(X_c^s)$ represents the Digital Number (DN) value of PIF in a subject image $f(X_c)$ , and $X_r^s$ represents the DN value of PIF in a reference image.

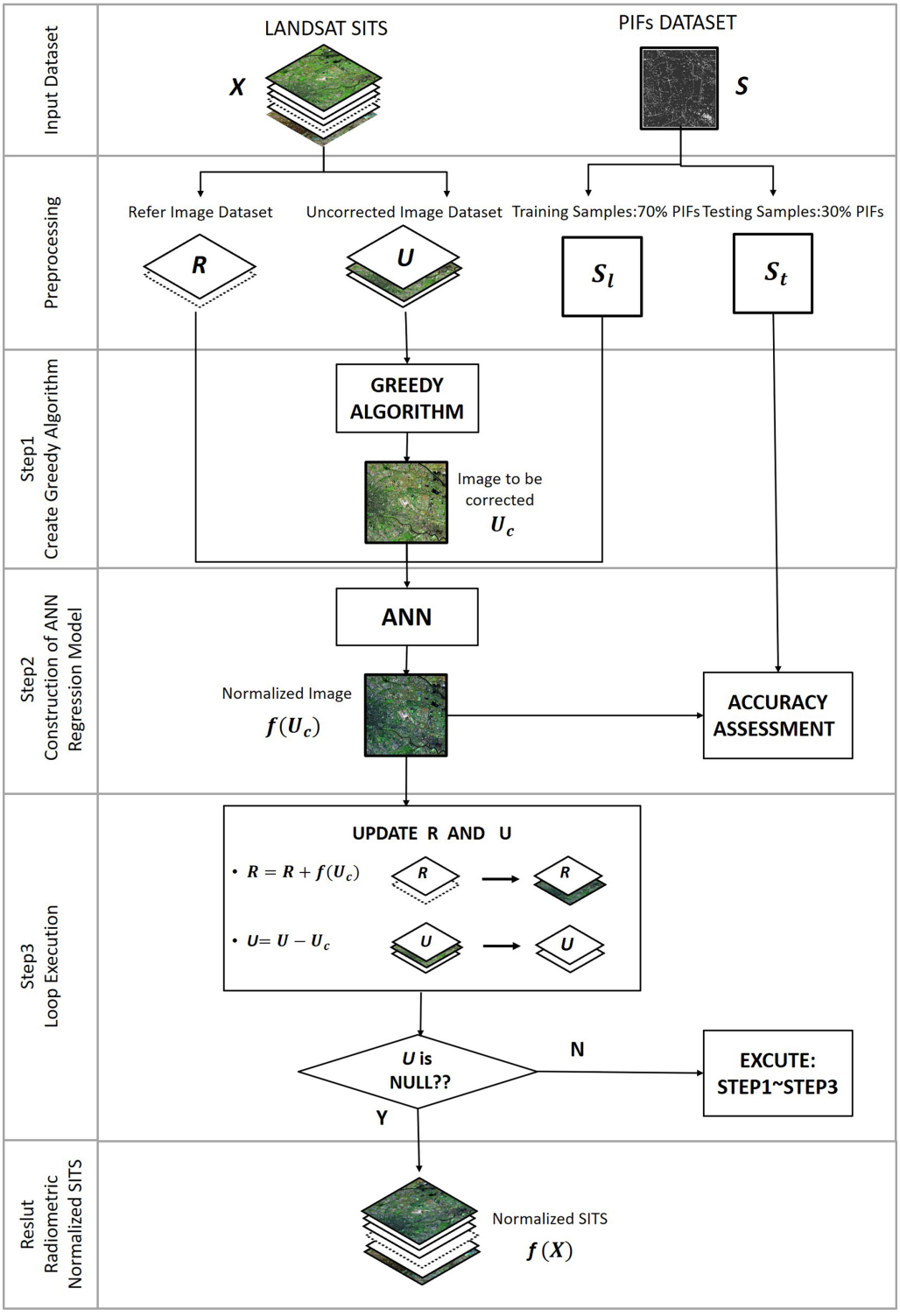


**Figure 1.** Flow diagram showing steps used by NMAG model in rediometric normalization for SITS.

When Equation 1 is used for the correction of SITS $X$, an image $X_r \in X$ is selected as the reference image, and then each image $X_i$ in $X$ is normalized with respect to the reference image $X_r$ in turn.The objective function $Q_r$ can be written as :

$$Q_r = min \sum_{i=1}^{n} \sum_{s \in S} [f(X_i^s) - X_r^s]^2 \quad (2)$$

where $n$ represents the number of images in $X$, and $f(X_i^s)$ represents the DN value of PIF in the image to be corrected $f(X_i)$. It can be easily found from Equation 2 that $Q_r$ cannot make sure the radiometric distortion between each pair of images in normalized SITS is minimum. Therefore, Wu et al. proposed an improved objective function $Q_G$ for the relative radiometric normalization of $X$, and $Q_G$ is expressed as [14]:

$$Q_G = min \sum_{i=1}^{n} \sum_{j=1}^{n} \sum_{s \in S} [f(X_i^s) - f(X_j^s)]^2 \tag{3}$$

Our NMAG method is based on this objective function, to achieve nonlinear radiometric normalization for SITS data by using artificial neural networks and greedy algorithms. The NMAG approach can be implemented using the following steps as shown in Figure 1.

Step1. Create a greedy algorithm [15]. In order to ensure that $Q_G$ can obtain the optimal solution, the greedy algorithm should be created to adopt the most greedy solution when implement the rediometric normalization of each image in a SITS.

SITS $X$ is divided into two groups, one as reference image dataset $R$ and the other as image dataset $U$ to be corrected:

$$X = R + U \tag{4}$$

The initial value of $R$ and $U$ can be given by:

$$R = \{\ \}\ and\ U = X \tag{5}$$

A clear and cloudless image $X_r$ is selected from SITS as the reference image, and then added $X_r$ to the reference image dataset $R$. Update $U$ according to Equation 6, then an image with smallest rediometric distortion from $R$ is selected from $U$ as the next image to be corrected $U_c$. The selection of $U_c$ can be given by Equation 7.

$$R = \{X_r\}\ and\ U = X - X_r \tag{6}$$

$$c = \underset{x \in [1,m]}{\operatorname{argmin}} (\sum_{i=1}^{k} \sum_{s \in S} (U_x^s - R_i^s)^2) \tag{7}$$

where $k$ represents the number of normalized images in $R$, $m$ represents the number of uncorrected images in $U$, and $s \in S$ represents the PIF in PIFs. $R_i^s$ represents the DN value of PIF in the $i$-th image of $R$ , and $U_x^s$ represents the DN value of PIF in the $x$-th image in $U$.

Next, implementing the rediometric normalization of $U_c$, and the local optimal solution $Q_c$ can be calculated by:

$$Q_c = min \sum_{i=1}^{k} \sum_{s \in S} [f(U_c^s) - R_i^s]^2 \tag{8}$$

where $f(U_c)$ represents the rediometric normalization result for $U_c$, and $f(U_c^s)$ represents the DN value of the PIF in $f(U_c)$ .

Step 2. Generate an ANN regression model. Linearity assumption of radiometric distortion in SITS is not precise, and nonlinear regression model may achieve more accurate normalization results of SITS. As a representative method of machine learning, ANN regression model has been widely used to solve nonlinear regression problems and has achieved significant results. The schematic diagram of ANN [16] is shown in Figure 2.

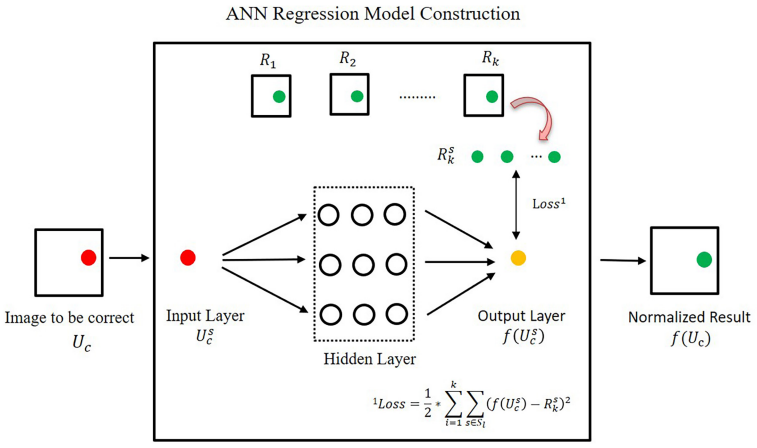


**Figure 2.** The schematic diagram of artificial neural network (ANN) regression model used in NMAG

In this study, PIFs were randomly divided into training sample set $S_l$ and test sample set $S_t$, accounting for 70% and 30% of total PIFs respectively. $S_l$ was used for the training of ANN regression model, and $S_t$ was used for the accuracy assessment of ANN regression model after training. As shown in Figure 2, ANN includes an input layer, an output layer and several hidden layers. The input layer is the DN value of the training samples in the image $U_c$ to be corrected, which is expressed as $U_c^s, s \in S_l$. The output layer is the radiometric normalization results $f(U_c^s), s \in S_l$.

The ANN regression model that is consisted of an input–output pair can be adjusted by the connection weights between the nodes by learning to memorize every one of the network learning and training samples. The magnitude of weights represents the importance of the link between the neurons to $f(U_c^s)$. The value of weights is initialized randomly, thus, the initial output is also random.The difference (i.e. error) between the generated output and a training set output is calculated and is fed back to the network, where it is used for connection-weight readjustment by Gradient Descent Algorithm (GDA) to minimize the error to within a predefined tolerance. In this way, the iteration calculation can reduced the error to a predetermined allowable range. The error estimation function can be expressed as:

$$LOSS = \frac{1}{2} * \sum_{i=1}^{k} \sum_{s \in S_l} (f(U_c^s) - R_i^s)^2 \tag{9}$$

where $k$ represents the number of images in $R$, and $R_i^s$ represents the DN value of PIFs in the $i$-th image in $R$.

Step 3. Loop execution. Added the corrected image $f(U_c)$ to reference image dataset R and remove $U_c$ from uncorrected image dataset $U$. The Update of $R$ and $U$ can be expressed as:

$$R = R + f(U_c) \; and \; U = U - U_c \tag{10}$$

where $f(U_c)$ is the radiometric normalization results of image $U_c$.

If there still exists images in the updated $U$, we execute the relative radiometric correction of the next image in the same way.

## 3. Materials

### *3.1. Study Area and Satellite Data*

Here, as an illustration of the application of NMAG modle, SITS with 21 high-quality landsat-8 satellite images covering an area of Tianjin were used in this study. The acquisition time of these images is from October 2017 to January 2019 and the average cloud cover

of images is 3.58%. The cost time of performing relative radiometric correction on entire images in SITS is too long, thus only 1000*1000 pixels were selected as the study area. The false color composite image of the study area is shown in Figure 3.

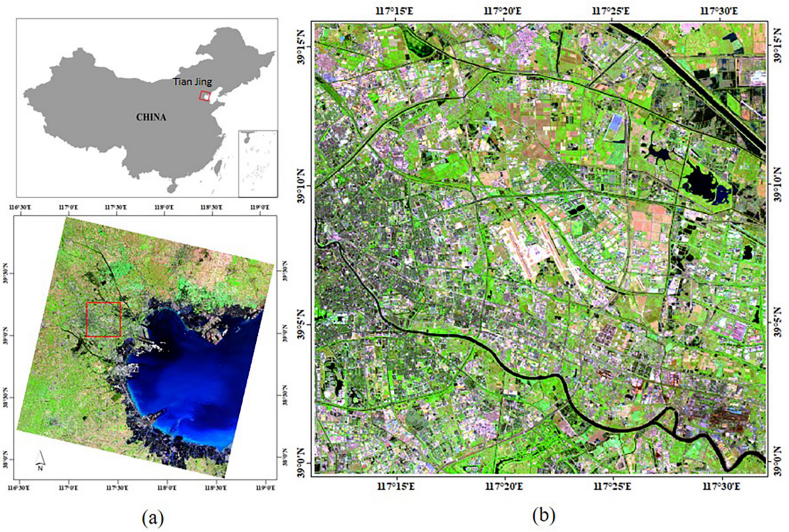


**Figure 3.** Overview of the study area: **(a)** the Landsat-8 image with Path=122 and Row=38 in the Worldwide Reference System (WRS), **(b)** The false color composite image in the study area (R: B7, G: B5, B: B4)

No further geometric correction is needed during image preprocessing because the positioning accuracy of these images obtained from the USGS [1] is less than one pixel. The false-color composite images of each temporal data in the SITS are given in Figure 4, and we can find from this figure that this area is rich in ground features, of which artificial buildings are mainly concentrated in the urban area of Tianjin, bare land is mainly distributed in suburbs of Tianjin, and road pixels are evenly distributed in the study area. The PIFs were mainly selected from pixels corresponding to this three types of ground features. Vegetation with intra-year seasonal changes are mainly distributed in suburbs of Tianjin, which can be selected to assess the accuracy of the radiometric normalization results of SITS.

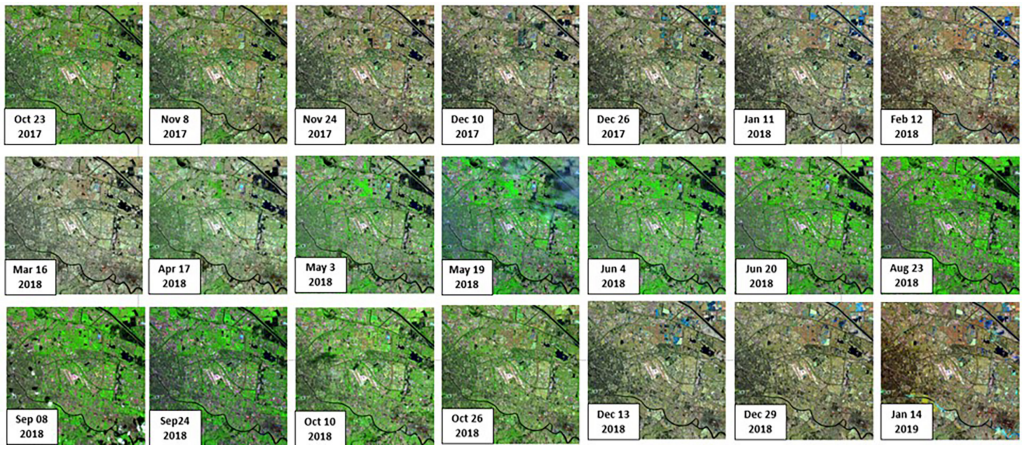


**Figure 4.** False-color composite image of SITS in the study area (R: B7, G: B5, B: B4)

The Pearson correlation coefficient matrix of landsat-8 SITS in the study area (Tianjin, China) from October 2017 to January 2019 is shown in Table 1 and Table 2. The larger

[1] https://glovis.usgs.gov

the Pearson Correlation Coefficient between different variables, the stronger the linear correlation of these variables, and vice versa. Table 1 shows that the range of Pearson Correlation Coefficient between images both acquired from October 2017 to December 2017 is 0.71~1.00, and the average value is 0.88, indicating that there exists a strong positive linear correlation between images which acquisition time is close. Table 2 shows that the range of Pearson Correlation Coefficient between image aquired from October 2017 to December 2017 and image acquired from October 2018 to December 2018 is 0.61~0.75, and the average value is 0.67, indicating that the linear correlation between images which acquisition time is far apart is weak. Due to there exist both linear and nonlinear radiation distortions between images in SITS in this area, the use of SITS in this area can be more beneficial to test the effectiveness of NMAG module.

**Table 1.** The Pearson correlation coefficient between images both acquired from October 2017 to December 2017

| | 2017-10-23 | 2017-11-08 | 2017-11-24 | 2017-12-10 | 2017-12-26 | mean_pccs |
|---|---|---|---|---|---|---|
| 2017-10-23 | 1.00 | 0.89 | 0.83 | 0.79 | 0.71 | 0.84 |
| 2017-11-08 | 0.89 | 1.00 | 0.91 | 0.88 | 0.81 | 0.90 |
| 2017-11-24 | 0.83 | 0.91 | 1.00 | 0.92 | 0.85 | 0.90 |
| 2017-12-10 | 0.79 | 0.88 | 0.92 | 1.00 | 0.89 | 0.90 |
| 2017-12-26 | 0.71 | 0.81 | 0.85 | 0.89 | 1.00 | 0.85 |
| mean_pccs | 0.84 | 0.90 | 0.90 | 0.90 | 0.85 | 0.88 |

**Table 2.** The Pearson correlation coefficient between image aquired from October 2017 to December 2017 and image acquired from October 2018 to December 2018

| | 2017-10-23 | 2017-11-08 | 2017-11-24 | 2017-12-10 | 2017-12-26 | mean_pccs |
|---|---|---|---|---|---|---|
| 2018-09-24 | 0.71 | 0.62 | 0.69 | 0.63 | 0.60 | 0.65 |
| 2018-10-10 | 0.73 | 0.66 | 0.75 | 0.68 | 0.65 | 0.69 |
| 2018-10-26 | 0.72 | 0.64 | 0.74 | 0.69 | 0.65 | 0.69 |
| 2018-12-13 | 0.70 | 0.65 | 0.73 | 0.70 | 0.65 | 0.69 |
| 2018-12-29 | 0.67 | 0.61 | 0.69 | 0.68 | 0.64 | 0.66 |
| mean_pccs | 0.70 | 0.64 | 0.72 | 0.68 | 0.64 | 0.67 |

### *3.2. The Preparation of PIFs*

PIFs refer to pixels with constant radiometric value in SITS, which were mainly selected from artificial buildings, roads or bare ground pixels. Using high-quality landsat-8 images of the study area can avoided the interference of clouds and shadows while selecting PIFs, which is more helpful to select high-quality PIFs. The SITS used here can be expressed as:

$$X = \{X_1, X_2, X_3, ..., X_n\} \tag{11}$$

The least squar method was used to estimate the best-fitting parameters ($k_p$ and $b_p$) of the time-series' DN value of pixel $p$ sorted in ascending order $DN_p^X$, and the distribution of $k_p$ values of the experimental area are shown in Figure 5 a. The slope of fitted line of PIFs $(k_s)$ is higher than that of water bodies and lower than that of vegetation [14]. Thus, the time-series' DN values of pixel $p$ sorted in ascending order can be given by Eq.(11) and the range of $k_s$ is expressed as:

$$DN_p^X = sort\ \{DN_p^{X_1}, DN_p^{X_2}, DN_p^{X_3}, ..., DN_p^{X_n}\}, p \in P \tag{12}$$

$$k_s \in [k_{Low}, k_{High}],\ s \in S \tag{13}$$

where $P$ represents all pixels in images in this area, $S$ represents selected PIFs, and $DN_p^X$ represents the time-series' DN value of pixel $p$ sorted in ascending order.

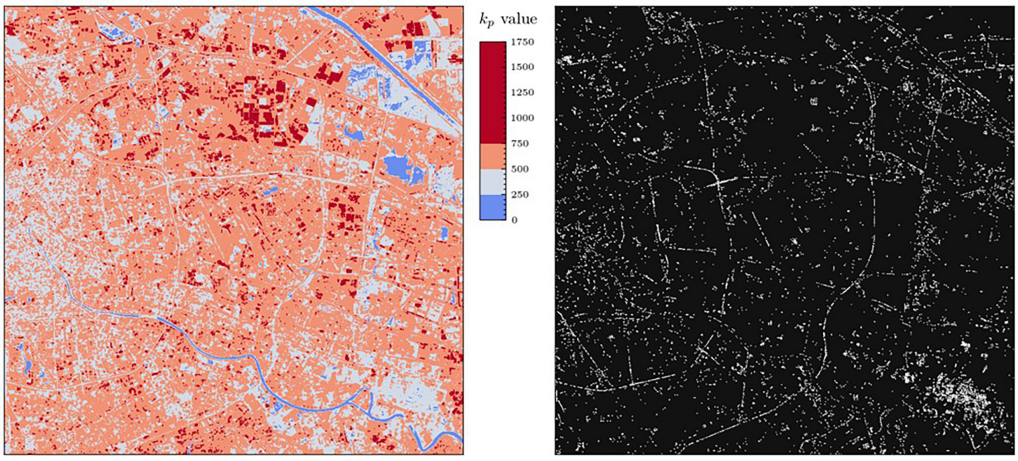


**Figure 5.** The selection result of Pseudo-invariant feature points (PIFs). **(a)** The distribution of $k_p$ values in the study area. The water bodies pixels in light blue; the road, bare land, and urban pixels in gray; and the vegetation pixels in orange or dark brown. **(b)** The selection result of PIFs. The white pixels represent PIF that is mainly selected from artificial buildings and bare lands.

As seen in Figure 5a, water bodies are displayed in light blue, artifical buildings and bare lands are showed in gray, and vegetation is expressed in orange or dark brown. The results indicates that the $k_p$ value of the water bodies is the lowest $(k_p < 250)$, the $k_p$ value of the vegetation is the highest $(k_p > 500)$, and the $k_p$ values of the artifical buildings and bare lands are between those of the water bodies and the vegetation $(250 < k_p < 500)$. PIFs represents pixels with unchange radiometric value over time, they were mainly selected from artificial buildings and bare lands. Thus, we set the thresholds of $k_s$ utilized in this paper to extract PIFs were 275 for $k_{Low}$ and 300 for $k_{High}$. The extraction results of PIFs are shown in Figure 5b, and white pixels represent PIFs, with a total of 12,515 pixels.

## 4. Results and Discussion

### *4.1. Experimental Results*

As an illustrative example, we applied NMAG model to the relative radiometric normalization of landast-8 SITS. Figure 6 shows the normalized results for SITS.

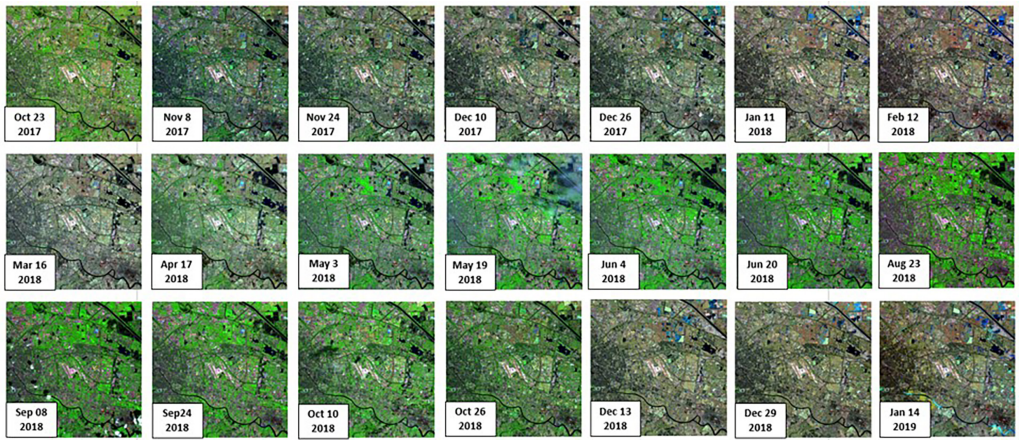


**Figure 6.** The relative radiometric normalized images in SITS

Figure 7 is a mosaic image composed of four normalized images taken from December

10 and 26, 2017, and December 13 and 29, 2018, respectively. In untreated images shown in Figure 4, there exists significant differences in color intensity and color saturation between images acquired on December 2017 and 2018. However, in normalized images shown in Figure 7a, we can see that all have similar radiometric intensity, hue and color saturation to each other.

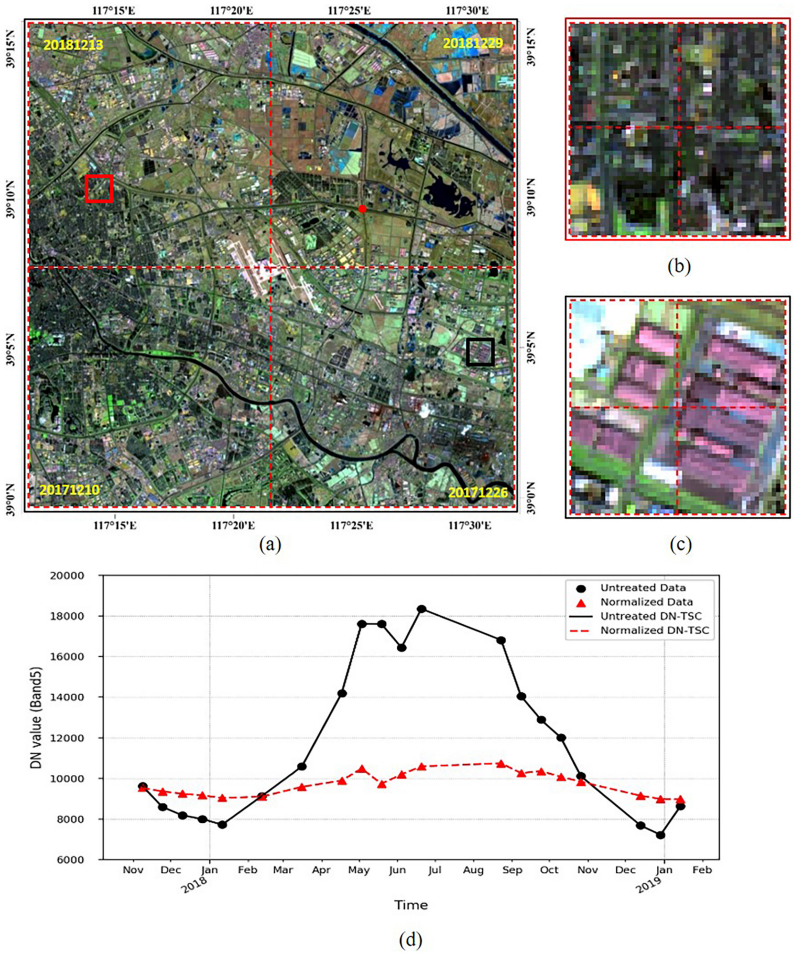


**Figure 7. (a)** The mosaic pattern composed of four normalized images taken from December 10 and 26, 2017, and December 13 and 29, 2018, respectively. The Resultant images have similiar color and color contrast to each other. **(b)**The mosaic pattern of the urban area, and the bundary of this area is marked in red box in figure **a**. **(c)** the mosaic pattern of the artificial building area, and the bundary of this area is marked in black box in figure **a**. **(d)** The comparison of time-series' curves of DN values (DN-TSC) from the near-infrared Band (Band 5) for the road pixel (marked in red point in figure**a**) before (marked in black line) and after (marked in red line) radiometric normalization.

Figure 7b and Figure 7c are two local area with complex ground features, including artificial bulidings, road and vegetation, are characterized with similiar color and color contrast. These results indicate that the radiometric distortion between different images caused by noise in SITS can be effectively suppressed by NMAG method.

Figure 7d shows the time-series' curve of DN values (DN-TSC) from the near-infrared Band (Band 5) of road pixels before and after radiometric normalization. The original DN-TSC fluctuate greatly,which indicates that the noise can conceal the actual variation of spectral characteristics from ground features. After radiometric normalization, the DN-TSC fluctuate slightly and nearly lie to a straight line. This indicates that NMAG effectively supresses the radiometric distortion between different images in SITS and result in DN values between images in SITS become more comparable.

Figure 8c shows the DN-TSC from the near-infrared Band (Band 5) of pixels in cropland

images before (black) and after(red) radiometric normalization. In general, there exists a single peak of DN-TSC during the entire corn growth period. According to information obtained from the website of Tianjin Agriculture and Rural Committee[2] and crop images during the growth period of corn (see Figure 8b), we know that corns in this area are generally sown in early June and are harvested at the end of October. This means that DN values of cropland pixel is similar to that of bare land pixel from November of the previous year to June of the current year, which should be hold on a fixed value theorically.

However, the original DN-TSC (marked in black line) fluctuate greatly from November 2017 to June 2018, and exist two peaks (May 19, 2018 and Sep 8, 2018 ) during the entire corn growth period. This means that the noises containded in the original DN-TSC led to large fluctuations and increased the difficulty of discovering the variation pattern of corn growth.

After radiometric normalization, the DN-TSC (marked in red line) fluctuate slightly from November 2017 to June 2018, demonstrating that NMAG method effectively minimizes the disturbtion of noise. A sigle peak (Sep 8,2018) existed in the normalized DN-TSC during the entire growth period, which indicates that NMAG can enhance the real time-series' characteristics for cropland pixels.

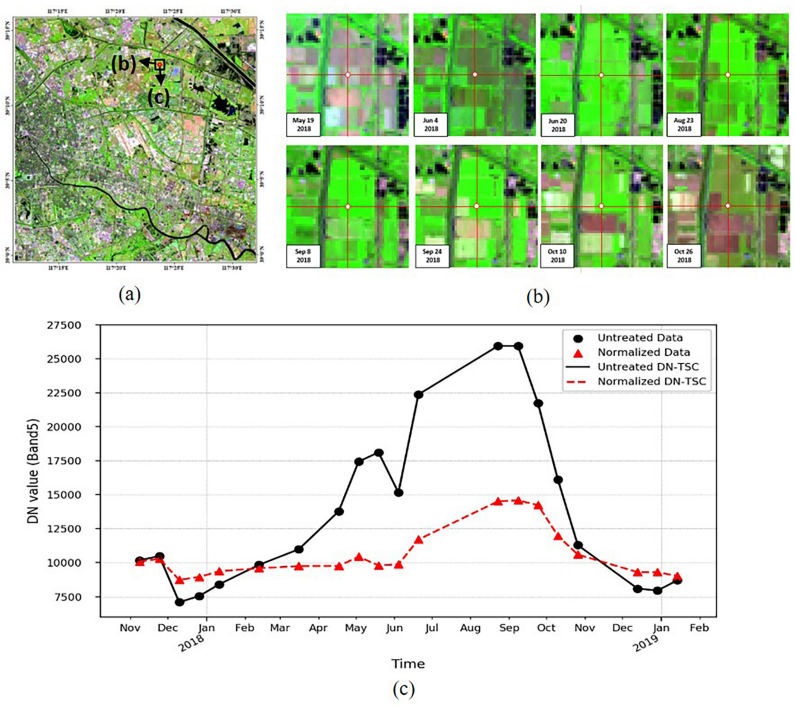


**Figure 8.** The relative radiometric normalization results of DN values of cropland pixel. **(a)** The location of cropland pixel and the boundary of crop images are marked in red point and black box, respectively. **(b)** The corpland images during the growth period of corn. **(c)** The Comparison of the DN-TSC from the near-infrared Band (band 5) for the cropland pixel before (marked in black line) and after (marked in red line) the radiometric normalization.

### *4.2. Comparison with other methods*

We compared NMAG module with other two contrast methods using the same data. The Contrast Method 1 (CM1) proposed by Sadeghi et al. is a nonlinear radiometric normalized based on the reference image to normalize the subject image [13]. When CM1 is used for the relative normalization of SITS, one image in SITS should be selected as a reference image first and then normalized other images to the reference image one by one. The Contrast Method 2 (CM2) proposed by Wu et al. is a rediometric normalization method

[2] http://nync.tj.gov.cn

for SITS based on linearity assumption [14]. In order to evaluate the accuracy of radiometric nomalization results obtained using different methods for SITS, we computed the root mean square error $RMSE(f(X_i), f(X_j))$ to measure the radiometric distortion between the normalized image $f(X_i)$ and the normalized image $f(X_j)$, which is can be calculated from Equation 14. The smaller the $RMSE$ value,the more accurate the radiometric normalization results of images.

$$RMSE(f(X_i), f(X_j)) = \sqrt{\frac{1}{N} \times \sum_{s \in S_t} [f(X_i^s) - f(X_j^s)]^2} \tag{14}$$

where $X_i$ represents $i$-th image in SITS, $X_j$ represents $j$-th image in SITS. $S_t$ represents the test samples of PIFs, $N$ represents the number of PIF in $S_t$ , $s$ represents the PIF in $S_t$, and $f(X_i^s)$ represents the DN value of PIF in the radiometric normalization result for image $X_i$.

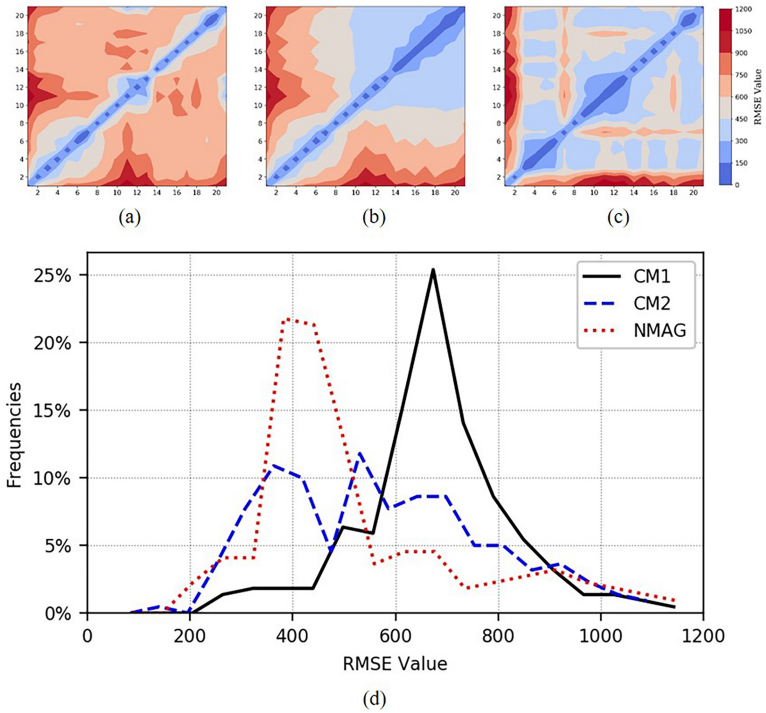


**Figure 9.** The error matrices and the frequency distribution curve of RMSE for the normalized results obtained using NMAG and two constrasting methods. As the color transitions from blue to red, the radiometric distortion increases.**(a)** The error matrices of RMSE obtained using CM1. **(b)** The error matrices of RMSE obtained using CM2. **(c)** The error matrices of RMSE obtained using NMAG. **(d)** The frequency distribution curve of RMSE obtained using NMAG and two constrasting methods.

Figure 9a-c shows error matrices of RMSE for the normalized results obtained using NMAG model and two constrasting methods with the same SITS data. In this figure, as the color transitions from blue to red, the RMSE increases. Compared with the error matrices of RMSE obtained using NMAG (see Figure 9c), more red pixels are observed in the error matrices of RMSE obtained using CM1 (see Figure 9a) and CM2 (see Figure 9b). This Qualitative analysis result shows that the error matrices of RMSE obtained using NMAG is generally distributed at low values.

Figure 9d shows the RMSE frequency distribution curve of NMAG (marked in red line) and other two methods (marked in black line and blue line,respectively). The RMSE between various images of CM1, CM2 and NMAG is concentrated around 700,550 and 400, respectively. Thus, the error of our method between images in SITS are significantly lower than that of CM1 and CM2. The comparison result demonstrates that NMAG method can

**Table 3.** Accuracy comparison of the $\mu_{RMSE}$ of NMAG, Contrast Method 1 (CM1) and Contrast Method 2 (CM2)

| Method | CM1[1] | CM2[2] | NMAG |
|---|---|---|---|
| $\mu_{RMSE}$ | 641.39 | 543.47 | 497.22 |

[1] CM1 proposed by Sadeghi et al. is a nonlinear radiometric normalization method based on the reference image to normalize the subject image.[13]
[2] The CM2 proposed by Wu et al. is a radiometric normalization method for SITS based on linearity assumption.[14]

reduce the radiometric distortion caused by noise between images in SITS more effectively than two contrasting methods, and obtain more accurate normalized results.

We further compared NMAG method with CM1 and CM2 by calculating the average of $RMSE(f(X_i), f(X_j))$. This parameter can be calculated by:

$$\mu_{RMSE} = \frac{1}{n^2} \sum_{i=1}^{n} \sum_{j=1}^{n} RMSE(f(X_i), f(X_j)) \tag{15}$$

where $n$ represents the number of images in SITS. $f(X_i)$ and $f(X_j)$ are respectively $i$-th and $j$-th image in normalized SITS.

Table 3 shows that the $\mu_{RMSE}$ of NMAG $(497.22)$ is significantly smaller than those of CM1 $(641.39)$ and CM2 $(543.47)$, and the accuracy of SITS obtained by using NMAG has increased by 22.4% and 8.5% toward CM1 and CM2, respectively. These results indicating that NMAG model can obtain more accurate SITS.

### *4.3. Application of NMAG to Vegetation Index*

Vegetaion index (VI) obtained from multi-band image data can better reflect the green vegetation status than DN value from single band data. Therefore, the time-series' vegetation index is often used in the field of land cover change monitoring, environmental monitoring and so on [17,18]. Considering the normalized difference vegetation index (NDVI) is the most frequently used VI in remote sensing applications [19], we further examine the application of NMAG to NDVI . The NDVI can be expressed as:

$$NDVI = \frac{\rho_{NIR} - \rho_R}{\rho_{NIR} + \rho_R} \tag{16}$$

Where $\rho_{NIR}$ is the top-of-atmosphere (TOA) reflectence from the near-infrared Band and $\rho_R$ is the top-of-atmosphere (TOA) reflectence from the red Band. With the help of metadata file $(\_MTL.txt)$, we can easily transform DN value into TOA reflectance. We used NMAG model to normalize the near-infrared band and the red band respectively, and normalized NDVI could be calculated by using normalized result of TOA reflectance of near-infrared Band and red Band.

Fig.10 shows the comparison of time-series' curve of NDVI values(NDVI-TSC) calculated from pixels in corpland images before (black) and after (red) the radiometric normalization. These two NDVI-TSC exist significant differences in details though they have the same trend. The fluctuation amplitude of NDVI-TSC obtained using NMAG is lower than that of untreated curve from November 2017 to May 2018. As mentioned in Section 4.1, the DN values of cropland pixel is similar to that of bare land pixel from November of the previous year to June of the current year, which should be hold on a fixed value theorically. This means the NDVI value of pixels should be also hold on a fixed value theorically from November 2017 to May 2018. The Reduction of fluctuation amplitude of NDVI-TSC indicates that NMAG can effectively decrease noises contained in different bands of SITS.

The time corresponding to the turning point of NDVI-TSC before and after the radiometric normalization is May 3, 2018 and May 19, 2018, respectively. This means that the corn sowing time corresponding to the untreated NDVI-TSC is between May 3,2018 and

May 19,2018, and the corn sowing time corresponding to the normalized NDVI-TSC by using NMAG is between May 19,2018 and June 4,2018. In reality, the corn sowing time is in early June, 2018 according to the information obtained from the website of Tianjin Agriculture and Rural Committee. The normalized result by using NMAG is fully matched the actual situation, showing that the timer-series' NDVI values obtained by using NMAG to normalize SITS data can better reflect the vegetation coverage, which is beneficial to improve the accuracy of remote sensing applications.

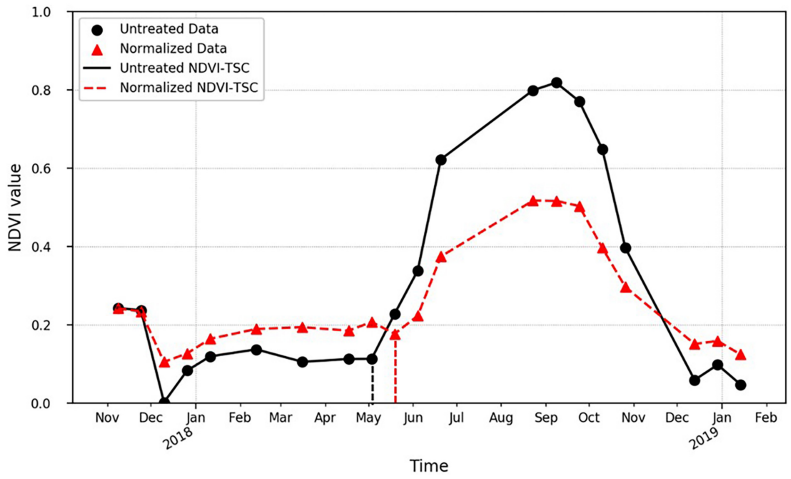


**Figure 10.** The Comparison of time-series'curve of NDVI values (NDVI-TSC) calculated from pixels in corpland images before (marked in black line) and after (marked in red line) the radiometric normalization.

## 5. Conclusions

In this paper, we propose a nonlinear radiometric noramlization method NMAG for SITS based on GA and ANN. This method can effectively supressed the noise contained in SITS, resulting in the gray values of images acquired at different time became more comparable. In the method, GA was used to determine the correction order of SITS and calculate the error between the image to be corrected and corrected images, which avoided the selection of a single reference image. ANN was used to obtain the optimal solution of error function, which minimized the radiometric distortion between images in SITS.

SITS composed of 21 Landsat-8 images in Tianjin City from October 2017 to January 2019 were used to test our method. The Resultant images have similiar color and color contrast to each other, and the normalized DN-TSC of the near-infrared Band (B5) obtain by using NMAG can better reflect the actual change of different features than the origin DN-TSC. In addition, We compared NMAG with other two existing methods (CM1 and CM2) using the same data. The result shows that the $\mu_{RMSE}$ of NMAG $(497.22)$ is significantly smaller than those of CM1 $(641.39)$ and CM2 $(543.47)$, and the accuracy of SITS obtained by using NMAG has increased by 22.4% and 8.5% toward CM1 and CM2, respectively. This indicates that NMAG can obtain more accurate SITS than other two constrasting methods.

Because the NDVI obtained from multi-band image data can better reflect the green vegetation status than DN value from single band data, We further analysed the application of NMAG to Vegetation Index. The NDVI-TSC obtained by using NMAG to normalize SITS data is fully matched the actual situation, indicating that NMAG can effectively reduce the rediometric distortion caused by noise in SITS so that we can obtain more precise time-series' NDVI values.

**Acknowledgments:** This work was supported by the NATIONAL NATURAL SCIENCE FOUNDATION OF CHINA grant number 41872214 and 42072232. The authors would like to express their gratitude to NASA and the USGS for providing remote sensing imageries (Landat-8 OLI images).

**Author Contributions:** All the authors made significant contributions to the work. Lejun Zou,Xiaohua Shen and Zhaohui Yin designed this research; Zhaohui Yin, Haoran Zhang and Jiayu Sun implemented the NMAG method and analyzed the results; Wenyi Zhang and Jiayu Sun designed and performed the comparison experiments between NMAG and other two contrasting methods; Zhaohui Yin wrote the paper; Xiaohua Shen and Lejun Zou gave insightful suggestions to the work.

**Conflicts of Interest:** The authors declare no conflict of interest.

## References


1. Zeng, L.; Wardlow, B.D.; Xiang, D.; Hu, S.; Li, D. A review of vegetation phenological metrics extraction using time-series, multispectral satellite data. *Remote Sens. Environ.* **2020**, *237*, 111511, doi:10.1016/j.rse.2019.111511.
2. Zhu, Z. Change detection using landsat time series: A review of frequencies, preprocessing, algorithms, and applications. *ISPRS J. Photogramm. Remote Sens.* **2017**, *130*, 370–384, doi:10.1016/j.isprsjprs.2017.06.013.
3. Vogelmann, J.E.; Xian, G.; Homer, C.; Tolk, B. Monitoring gradual ecosystem change using Landsat time series analyses: Case studies in selected forest and rangeland ecosystems.*Remote Sens. Environ.* **2012**, doi:10.1016/j.rse.2011.06.027.
4. Yang, X.; Lo, C.P. Relative radiometric normalization performance for change detection from multi-date satellite images. *Photogramm. Eng. Remote Sensing*.**2000**.
5. Canty, M.J.; Nielsen, A.A. Schmidt, M. Automatic radiometric normalization of multitemporal satellite imagery. *Remote Sens. Environ.* **2004**, *91*, 441–451, doi:10.1016/j.rse.2003.10.024.
6. Yang, Z.; Mueller, R. Unbiased histogram matching quality measure for optimal radiometric normalization. *In Proceedings of the American Society for Photogrammetry and Remote Sensing - ASPRS Annual Conference 2008 - Bridging the Horizons: New Frontiers in Geospatial Collaboration*; **2008**.
7. Biday, S. G.; Bhosle, U. Radiometric Correction of Multitemporal Satellite Imagery. *Journal of Computer Science* .**2010**, *6(9)*, 1027-1036. https://doi.org/10.3844/jcssp.2010.1027.1036
8. Du, Y.; Teillet, P.M.; Cihlar, J. Radiometric normalization of multitemporal high-resolution satellite images with quality control for land cover change detection. *Remote Sens. Environ.* **2002**, *82*, 123–134, doi:10.1016/S0034-4257(02)00029-9.
9. Schott, J.R.; Salvaggio, C.; Volchok, W.J. Radiometric scene normalization using pseudoinvariant features. *Remote Sens. Environ.* **1988**, *26*, 1–16, doi:10.1016/0034-4257(88)90116-2.
10. Du, Y.; Cihlar, J.; Beaubien, J.; Latifovic, R. Radiometric normalization, compositing, and quality control for satellite high resolution image mosaics over large areas. *IEEE Trans. Geosci. Remote Sens.* **2001**, *39*, 623–634, doi:10.1109/36.911119.
11. Olthof, I.; Pouliot, D.; Fernandes, R.; Latifovic, R. Landsat-7 ETM+ radiometric normalization comparison for northern mapping applications. *Remote Sens. Environ.* **2005**, *95*, 388–398, doi:10.1016/j.rse.2004.06.024.
12. Liu, S.H.; Lin, C.W.; Chen, Y.R.; Tseng, C.M. Automatic radiometric normalization with genetic algorithms and a Kriging model. *Comput. Geosci.* **2012**, *43*, 42–51, doi:10.1016/j.cageo.2011.12.016.
13. Sadeghi, V.; Ebadi, H.; Ahmadi, F.F. A new model for automatic normalization of multitemporal satellite images using Artificial Neural Network and mathematical methods. *Appl. Math. Model.* **2013**, *37*, 6437–6445, doi:10.1016/j.apm.2013.01.006.
14. Wu, W.; Sun, X.; Wang, X.; Fan, J.; Luo, J.; Shen, Y.; Yang, Y. A long time-series radiometric normalization method for landsat images. *Sensors (Switzerland).* **2018**, *18*, 1–22, doi:10.3390/s18124505.
15. Edmonds, J. Matroids and the greedy algorithm. *Math. Program.* **1971**, *1*, 127–136, doi:10.1007/BF01584082.
16. Jain, A.K.; Mao, J.; Mohiuddin, K.M. Artificial neural networks: A tutorial. Computer *(Long. Beach. Calif).* **1996**, *29*, 31–44, doi:10.1109/2.485891.
17. Zhang, X.; Friedl, M.A.; Schaaf, C.B.; Strahler, A.H.; Hodges, J.C.F.; Gao, F.; Reed, B.C.; Huete, A. Monitoring vegetation phenology using MODIS. *Remote Sens. Environ.* **2003**, *84*, 471–475, doi:10.1016/S0034-4257(02)00135-9.
18. Schultz, M.; Clevers, J.G.P.W.; Carter, S.; Verbesselt, J.; Avitabile, V.; Quang, H.V.; Herold, M. Performance of vegetation indices from Landsat time series in deforestation monitoring. *Int. J. Appl. Earth Obs. Geoinf.* **2016**, *52*, 318–327, doi:10.1016/j.jag.2016.06.020.
19. Rouse, J.W.,Jr; Haas, R.H.; Schell, J.A.; Deering, D.W. Monitoring Vegetation Systems in the Great Plains with Erts. *Nasa Special Publication*. **1974**. *351(20)*. 309-317.